Understanding the thermomechanical behavior of a TATB-based explosive via microstructure-level simulations. Part I: Microcracking and viscoelasticity

Hervé Trumel, François Rabette, François Willot, Renald Brenner, Emmanuelle Ongari, Maxime Biessy, Didier Picart

Understanding the thermomechanical behavior of a TATB-based explosive via microstructure-level simulations. Part I: Microcracking and viscoelasticity.

H. Trumel[1], F. Rabette[1,2], F. Willot[2], R. Brenner[3], E. Ongari[1], M. Biessy[1], D. Picart[1]

[1] *CEA, DAM, Le Ripault, F-37260 MONTS, France.*
[2] *MINES ParisTech, PSL – Research University, CMM – Centre for Mathematical Morphology, 35, rue St Honoré, F-77300 Fontainebleau, France.*
[3] *Sorbonne Université, Institut Jean le Rond ∂'Alembert, 4, place Jussieu, F-75252 PARIS Cedex 05, France.*

Abstract. In view of a better understanding of the thermomechanical behavior of pressed explosives, a Fourier-based computational tool is used to perform numerical homogenization and compare predictions to experimental macroscopic properties. This is first done in a purely thermoelastic context on simplified polycrystalline virtual microstructures, then extended to cracked polycrystalline ones. A further extension is proposed, aiming at predicting the nucleation and propagation of (micro)-cracks. Besides, a mean-field (self-consistent) approach is also followed, providing accurate thermoelastic predictions. It is currently being extended to account for linear (non-ageing) viscoelasticity of the binder. The study of irreversible deformation mechanisms of the TATB crystal, in view of their incorporation in the full-field tool, is the subject of the companion paper.

1. Introduction

Pressed explosives display a so-called « quasi-brittle » quasi-static thermomechanical behavior (see, e.g. **Le et al., 2010**), similar to that of concrete or soft rocks, and characterized by (i) at low stress triaxiality (i.e. low pressure): a low strain to fracture, a large dissymmetry between the fracture stress in tension and compression, (ii) a strong sensitivity to stress triaxiality and a brittle-to-ductile transition, and (iii) a ductile behavior at high stress triaxiality. Although containing quite small volume fractions of polymeric binder, they also display a marked viscoelastic effect (**Picart and Brigolle, 2010**). Among this class of materials, TATB-based pressed explosives additionally exhibit an atypical feature, namely irreversible thermal expansion, generally attributed to the strong anisotropy of the TATB single crystal (**Kolb and Rizzo, 1979**).

The present paper is devoted to such a material, containing a few percent of an amorphous polymeric binder, isostatically pressed to less than 3% porosity. It has been submitted to a variety of loadings (uniaxial tension, uniaxial, biaxial and triaxial compression, simple shear, etc,) parameterized by temperature and strain rate, and can be considered to be quite well characterized. However, it is yet difficult to provide clear and quantitative interpretations to the available set of stress-strain curves, and physically-based thermomecanical modeling remains out of reach at the moment.

In order to endeavor to fill the gap, a two-fold theoretical and numerical scale transition approach has been followed, combining a Fourier-based full-field computational tool (**Gasnier et al., 2018a**, **b**) and the capabilities of mean-field theories (**Gallican et al., 2017, 2018**). Given the complexity of the task, this is being done by introducing progressively the various physical, possibly anisotropic, mechanisms at stake, namely thermoelasticity, inter- and transgranular microcracking, binder viscoelasticity and TATB crystal (visco)-plasticity, within an as realistic as possible description of the microstructure of the considered material.

2. Thermomechanical response

Fig. 1 displays in black and in the inset an example of the quasi-static (3×10^{-4} s^{-1}) uniaxial (stress) cyclic compression of the studied material at room temperature. This plot shows progressive softening, together with unloading-reloading hysteresis loops typical of quasi-brittle (i.e. concrete-like) materials. Strong time-dependence appears clearly during the relaxation (constant strain) and recovery (zero stress) phases.

Superimposed in gray on this plot, an example of the quasi-static triaxial cyclic compression at room temperature and 200 MPa confining pressure. The effect of pressure is obvious: the response is much more

ductile, and the maximum stress is ~2.7 times higher than in the uniaxial case and occurs at ~36% longitudinal strain, to be compared with ~1.5% under uniaxial conditions.

Fig. 2a shows an example of the thermal expansion response at high temperature, i.e. above the glass transition temperature of the binder. Irreversibility is clearly displayed, well known in the community as "ratchet growth" (see, e.g. **Kolb and Rizzo, 1981**; **Thompson et al., 2018**), and results in an increase of the explosive porosity. Crossing the binder glass transition temperature (~100°C) results in a spectacular increase of the thermal expansion coefficient. A second cycle provokes an additional but less pronounced dilatancy, well described in the specialized literature. It is also remarkable that the two cooling curves are strictly identical, apart from a vertical (dilatancy) shift.

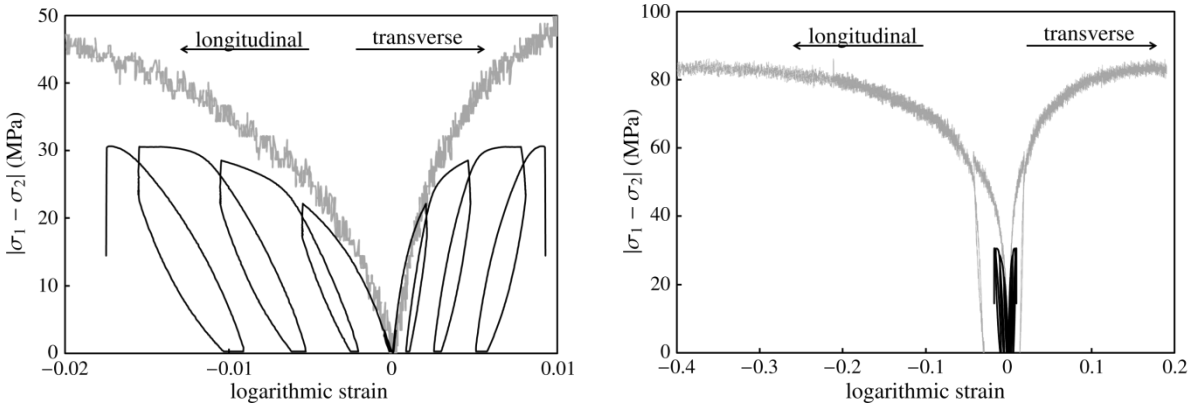

Fig. 1: Compression stress-strain curves (black: uniaxial - grey: triaxial with 200 MPa confining pressure)
a (left): detail of the uniaxial case – **b** (right): full scale triaxial case

Fig. 2b, relative to low temperature thermal cycles, shows an entirely different picture. Cooling is firstly linear, then nonlinear after a threshold is reached at ~5°C. Reheating begins with a linear phase, associated with a thermal expansion coefficient lower than in the initial state. The initial coefficient is then progressively recovered. Further thermal cycles show that the memory of the previous cycles is kept, at least partially. Dilatancy is again observed, but amounts to much lower values than in the high temperature case.

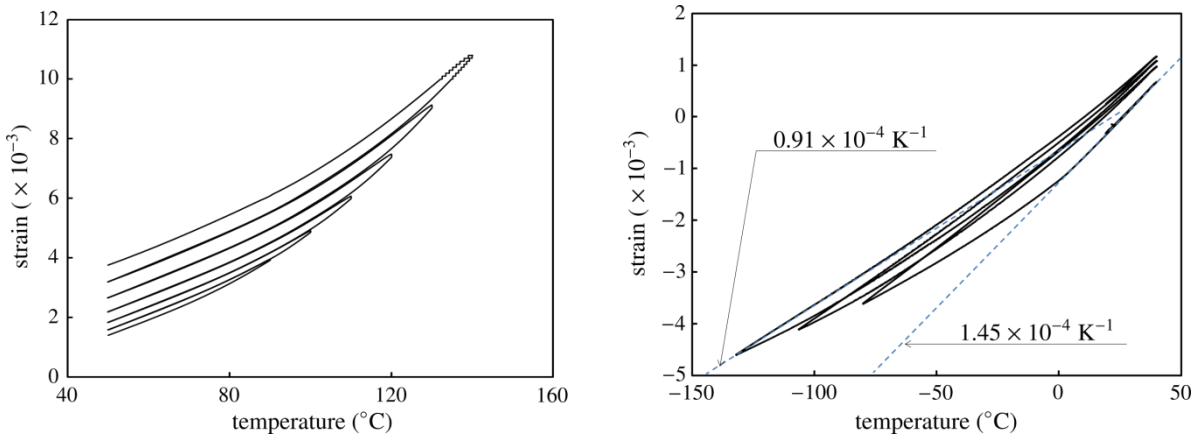

Fig. 2: Cyclic thermal expansion experiments.
a (left): high temperature - **b** (right): low temperature.

High and low temperature cycling experiments therefore display strongly differing responses. From additional experiments (not shown, see **Gasnier et al., 2018b**), is it known that ay high temperature, most of the dilatancy occurs above the binder glass transition, thus suggesting a grain-binder debonding (i.e. intergranular) process. At low temperature, the decrease of the thermal expansion coefficient, followed by its recovery upon reheating, resembles a unilateral crack opening-closure effect, thus suggesting a microcracking process.

Moreover, the linear part of the thermogram between, say, 5 and 70°C, indicates a reproducible volumetric room temperature thermal expansion coefficient of 1.45×10^{-4} K^{-1}. This value is significantly lower than that of the TATB single crystal (**Kolb and Rizzo, 1981** ; **Sun et al., 2010**). This means that, well below the binder glass temperature, strong internal stresses develop upon heating and cooling as well, and oppose to the

thermal expansion of individual TATB crystals. This is attributed (see **Kolb and Rizzo, 1981**; **Gee et al., 2007**) to the combination of the strong elastic and thermal expansion anisotropy of the TATB crystal, on the one hand, and to the random orientation of crystals in the explosive, on the other hand: each crystal tends to oppose to the expansion of neighboring ill-oriented crystals. Of course, this can only occur if the binder is able to transmit stresses across interfaces, i.e. below the binder glass transition temperature.

3. Microstructure and microstructure representation

Fig. 3a shows the microstructure of the studied material using polarized light optical microscopy. Fig. 3b shows a SEM (back-scattered electron imaging) micrograph after etching the polished surface with a solvent of the binder, thus revealing grain boundaries. The material appears as a polycrystal with many defects, among which pores, deformation bands (possibly twins), and microcracks, and grains are most often single crystals, sometimes bi-cristals. The deformation bands are completely absent from the initial powder (not shown), thus witnessing heavy (plastic) deformation sustained by the TATB grains during the pressing process.

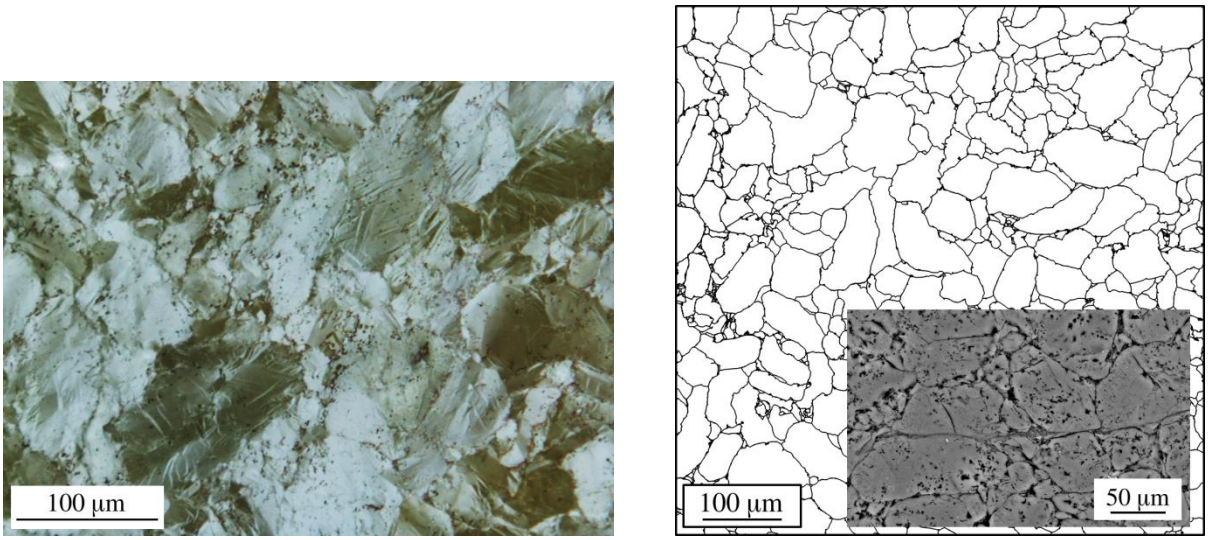

Fig. 3: Microstructure of the studied material
a (left): optical microscopy (reflected polarized light)
b (right): image segmented from scanning electron microscopy (back-scattered electrons), after surface etching (inset).

Although the binder is not resolved on optical micrographs, it was detected using EDS, Raman spectroscopy, NMR and image analysis (**Palmas et al., 2016**). The resolution of these techniques is not sufficient to guarantee the presence of binder around each individual grain, but most grains should be separated by a thin layer of binder, of average size around 200 nm as an order of magnitude.

In order to perform full field simulations on representative microstructures, digital three-dimensional images are needed. Unfortunately, because of the low X-ray absorption contrast in this material, laboratory microtomographs could not be obtained. Therefore, 3D virtual microstructures have been constructed (**Ambos et al., 2015** ; **Gasnier et al., 2015**) via tessellation models, i.e. Voronoi, Laguerre and Johnson-Mehl ones, identified to mimic as accurately as possible the main 2D morphological characteristics (grain size and aspect ratio distributions) of the studied material measured on segmented SEM images. Figure 4a shows a 2D slice of a realization of a Johnson-Mehl tessellation model, for which the spatio-temporal coordinates of grain germs are chosen according to a Poisson random model, and the grains growth according to a deterministic anisotropic law (**Gasnier et al., 2015**).

In a second step, the binder will be represented by applying a morphological erosion of the grains of Fig. 4a, using a structural element of a given diameter, the latter being representative of the thickness of the binder layer, supposedly uniform around the grains (Fig. 4b).

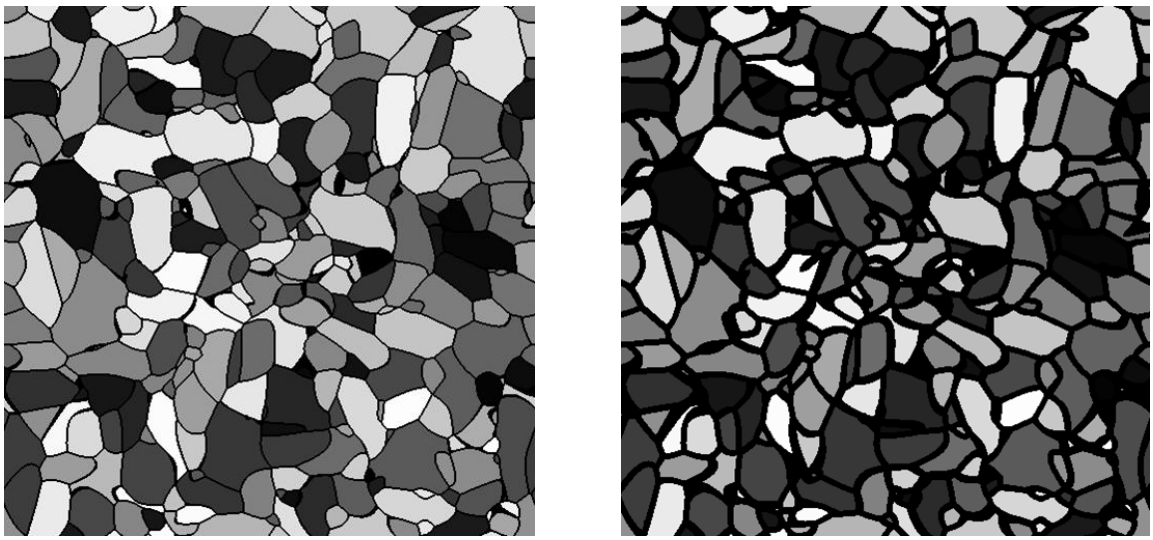

Fig. 4: 2D slices of virtual microstructure random tessellation models.
a (left): Johnson-Mehl model - **b** (right): Johnson-Mehl model with 6 voxel thick binder.

4. Full-field determination of effective linear thermoelastic properties

The tessellation illustrated in Fig. 4a is first considered to represent the material microstructure. This implies that porosities, microcracks, deformation twins and the binder are neglected, that TATB grains are assumed to be single crystals, and that grain boundaries are supposed to be perfectly bonded.

4.1. Problem formulation

Under these assumptions, numerical (i.e. full-field) periodic homogenization can be performed by solving the following problem. Consider a linear (anisotropic) thermoelastic representative volume element (RVE) Ω bounded by its boundary $\partial\Omega$, submitted to a macroscopic strain $\bar{\boldsymbol{E}}$ and a uniform temperature field $\Delta T = T - T_0$, with periodic boundary conditions. Then, the problem may be stated as follows:

- local linear thermoelastic behavior: $\sigma_{ij} = \mathbb{C}_{ijkl}\ \epsilon_{kl} - \alpha_{kl}\Delta T$,
- local equilibrium: $\sigma_{ij,j} = 0$,
- boundary conditions: $u_i(\boldsymbol{x} + \mathbf{L}_\alpha \boldsymbol{e}_\alpha) = u_i(\boldsymbol{x})$, $\sigma_{ij} n_j(\boldsymbol{x}) = -\sigma_{ij} n_j(\boldsymbol{x} + \mathbf{L}_\alpha \boldsymbol{e}_\alpha)$,
- homogenization: $\int_\Omega \epsilon_{ij} dV = \bar{E}_{ij}$, $\Sigma_{ij} = \int_\Omega \sigma_{ij} dV$,

where T_0 is a reference temperature, $\boldsymbol{\sigma}$ is the stress field, $\mathbb{C}$ and $\boldsymbol{\alpha}$ are the local elastic and thermal expansion tensors, $\boldsymbol{u}$ is the displacement field, $\boldsymbol{x}$ the position vector of any material point inside Ω, L_α ($1 \leq \alpha \leq 3$) is the length of Ω along the $\boldsymbol{e}_\alpha$ direction, $\boldsymbol{n}$ is the outward normal of $\partial\Omega$, $\boldsymbol{\epsilon}$ is the strain field and $\boldsymbol{\Sigma}$ is the macroscopic stress tensor.

4.2. FFT method and algorithm

In the context of periodic homogenization, **Moulinec and Suquet, 1994** proposed an elegant way to solve for the local fields and effective properties via fast Fourier transform (FFT), which is now briefly outlined. While the above-described problem considers locally varying elastic properties $\mathbb{C}(\boldsymbol{x})$, the FFT method proposes to re-formulate it as with uniform "auxiliary" elastic properties $\mathbb{C}^0$ as follows (see also **Anglin et al., 2014**):

$$\begin{cases} \sigma_{ij} = \mathbb{C}^0_{ijkl}\epsilon_{kl} + \tau_{ij} \\ \sigma_{ij,j} = 0 \end{cases} \tag{1}$$

where $\boldsymbol{\tau}$, called the "polarization" field, is by definition $\tau_{ij} = \mathbb{C}_{ijkl}(\boldsymbol{x}) - \mathbb{C}^0_{ijkl}\ \epsilon_{kl}(\boldsymbol{x}) - \mathbb{C}_{ijkl(x)}\alpha_{kl}(\boldsymbol{x})\Delta T$.
Then, the solution of problem (1) is given by:

$$\delta\epsilon_{ij}(\boldsymbol{x}) = -\int_{\Omega} \Gamma^0_{ijkl}(\boldsymbol{x}-\boldsymbol{x}')\tau_{kl}(\boldsymbol{x}')d\boldsymbol{x}' \tag{2}$$

where $\delta\epsilon_{ij}(\boldsymbol{x}) = \epsilon_{ij}(\boldsymbol{x}) - \bar{E}_{ij}$ is the local strain fluctuation, and $\boldsymbol{\Gamma}^0$ is the periodic Green operator associated with $\mathbb{C}^0$. The convolution integral appearing in Eqn. (2) transforms into a simple product in the Fourier space, in which Eqn. (2) becomes simply:

$$\delta\hat{\epsilon}_{ij}(\boldsymbol{\xi}) = -\hat{\Gamma}^0_{ijkl}(\boldsymbol{\xi})\hat{\tau}_{kl}(\boldsymbol{\xi}) \tag{3}$$

where $\boldsymbol{\xi}$ is the Fourier wave vector. Since the Green operator is known analytically in the Fourier space, a fixed-point algorithm can be used to solve Eqn. (3) iteratively, beginning with $\delta\hat{\epsilon}_{ij}(\boldsymbol{\xi}) = 0$, and the strain fluctuation field is sought as a truncated Fourier series. This algorithm evaluates the stress and polarization fields in the real space and the strain fluctuation field in the Fourier space, such that Fourier and inverse Fourier transforms represent the main computational effort. Its strong advantages are its high efficiency and low memory demand while, as a relatively recent method, its major drawback is that it is not as developed as the finite element method, especially for nonlinear behavior.

4.3. Results

In what follows, the thermoelastic properties $\mathbb{C}$ and $\boldsymbol{\alpha}$ of the TATB crystal are given in GPa and in 10^{-6} K^{-1} respectively by (**Bedrov et al., 2009** ; **Sun et al., 2010**):

$$\mathbb{C} = \begin{pmatrix} 65.7 & 18.5 & 4.0 & -0.2 & -1.0 & 1.0 \\ & 62.0 & 5.0 & 0.6 & -0.5 & 1.0 \\ & & 18.3 & 0.2 & -0.4 & -0.4 \\ & & & 1.4 & 0.1 & 0.3 \\ & \text{sym.} & & & 0.68 & 0.4 \\ & & & & & 21.6 \end{pmatrix} \quad \boldsymbol{\alpha} = \begin{pmatrix} 12.29 & -0.95 & 19.41 \\ & 9.022 & -37.39 \\ \text{sym.} & & 166.2 \end{pmatrix} \tag{4}$$

showing very strong shear and thermal expansion anisotropies.

With these data at hand, seven calculations with independently applied macroscopic strains calculations on a 512^3 voxels domain containing around 2800 randomly oriented TATB grains allow obtaining the complete effective elastic and thermal expansion tensors. The effective tensors are shown to be quasi-isotropic, with effective bulk and shear moduli and volumetric thermal expansion coefficient of 17 GPa, 6.8 GPa and $1.48\text{x}10^{-4}$ K^{-1} respectively, to be compared to 7.2 GPa, 2.7 GPa and $1.45\text{x}10^{-4}$ K^{-1} determined experimentally.

The effective thermal expansion coefficient agrees remarkably well with experimental values. Besides, the strong discrepancy between predicted and measured effective elastic moduli can be attributed neither to the presence of the binder nor to that of pores: accounting for both yielded bulk and shear moduli of 14.8 and 5.7 GPa respectively. The value of the bulk modulus agrees well with high pressure hydrostatic results (not shown, see **Gasnier et al., 2018b**), thus giving relevance to the present approach.

5. Microcracking

The only way to explain the remaining discrepancy is to invoke the presence of open (micro)-cracks in the initial state. Since cracking is also at work under low triaxiality loading and strongly suspected under thermal loading, the next step is to include this mechanism within the full-field FFT approach.

5.1. *Evaluating the effect of randomly oriented microcrack populations*

This is done by inserting various randomly oriented populations of either intergranular of transgranular microcracks in the perfect polycrystal, and evaluating the resulting effective thermoelastic properties of the cracked polycrystal. Given the random orientation of microcracks, the effective properties remain isotropic. Fig. 5a and b display respectively the evolutions of the effective bulk and shear moduli with the density of microcracks defined as follows (**Budiansky and O'Connell, 1976**):

$$\eta = \frac{2\mathcal{N}}{\pi}\left\langle \frac{A^2}{P} \right\rangle \tag{5}$$

where $\mathcal{N}$ is the number of cracks, A and P the area and perimeter of each crack, respectively, and $\langle\ \rangle$ stands for the average over all cracks.

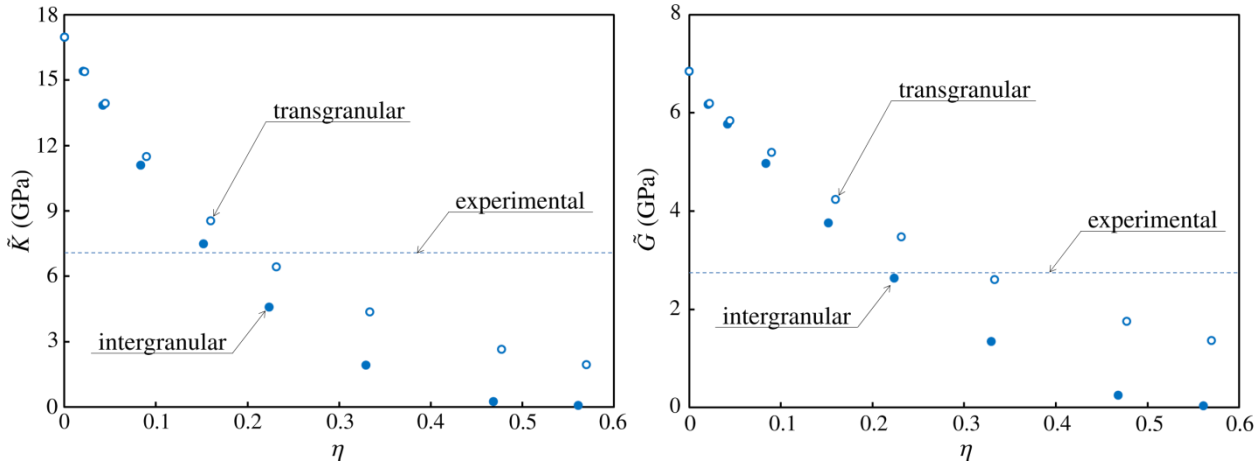

Fig. 5: Effective bulk and shear moduli versus microcrack density
a (left): bulk modulus – **b** (right): shear modulus.

Notice that at a crack density of ~0.5, the effective elastic moduli for the intergranular case vanish, thus indicating percolation and fracture. Figs. 5a and b also indicate the experimental values (dashed blue line). Obtaining a common value (~0.2) of the crack density for both the effective bulk and shear moduli is only possible for the intergranular case. Therefore, one concludes that the material is very likely to contain intergranular microcracks in its initial state.

5.2. *Effective thermal expansion coefficient*

Fig. 6a shows the effect of microcracking on the effective thermal expansion coefficient. The effect is negligible below the percolation threshold, above which the effective expansion coefficient increases sharply and encompasses that of the single crystal. Therefore, for the above determined initial crack density of 0.2, there is no measurable effect on thermal expansion, explaining why the polycrystal prediction is so accurate.

However, this does not explain the decrease of the thermal expansion coefficient at low temperature. It must therefore be concluded that the assumption of random orientation of microcracks is not valid in this case, but rather that their orientation must be correlated with those of crystals (transgranular case). Fig. 6b displays the results obtained for three cases, namely cracks developing in the graphitic plane of the TATB crystal, perpendicularly to it, and the uncorrelated case seen previously. It appears clearly that the decrease of the effective thermal expansion coefficient is obtained for cracks developing in the graphitic plane of the TATB crystal. This can also be interpreted following **Rosen and Hashin, 1970**, who showed that the effective thermal expansion coefficient of a polycrystal depends on the elastic and thermal expansion anisotropy. Introducing a microcrack in a crystal can be interpreted as a modification of the local thermoelastic tensors of the crystal. If the crack lies along the graphitic planes of the crystal, the elastic anisotropy increases, thus decreasing the effective thermal expansion coefficient, consistently with the numerical findings of Fig. 6b (**Gasnier et al., 2018b**). This interpretation also suggests an asymptotic value of the effective thermal expansion coefficient.

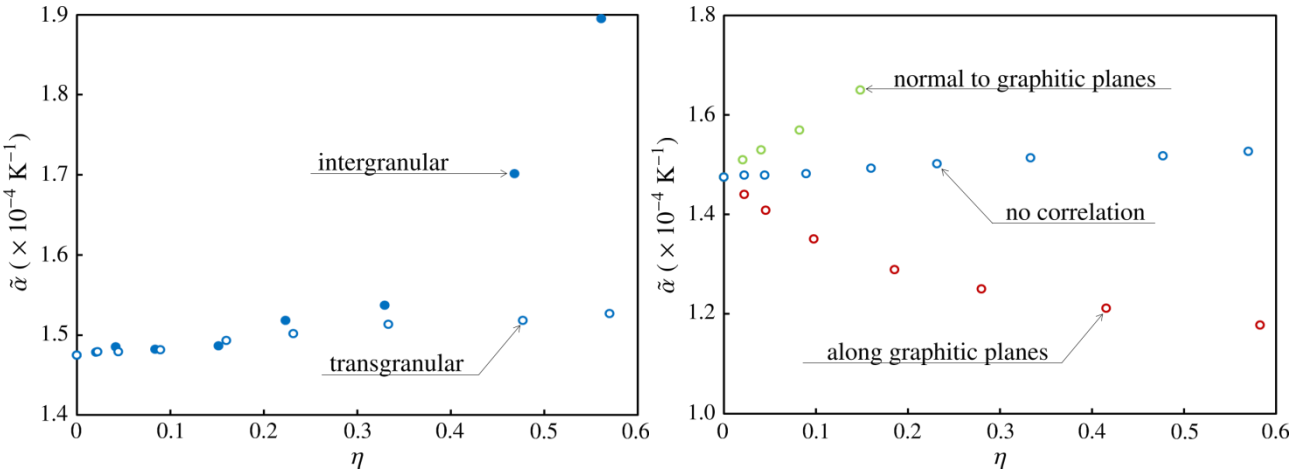

Fig. 6: Influence of microcracking on the effective thermal expansion coefficient
a (left): randomly oriented microcracks – **b** (right): correlated to crystallographic orientations (transgranular).

6. A model for local fracture

Up to now, only fixed populations of cracks have been considered. Ongoing work is being devoted to the implementation of a model able to describe the appearance and propagation of new cracks, the first results being presented below.

6.1. Proposed approach

The starting point is (i) to assume first that only brittle fracture is involved, (ii) to consider infinitesimal deformations, such that $\boldsymbol{\epsilon} = \mathrm{sym}(\nabla \boldsymbol{u})$, $\boldsymbol{u}$ being the displacement and ∇ the gradient operator, and (iii) to rely on the variational approach to brittle fracture proposed by **Francfort and Marigo, 1998**. These authors consider that at any time, fracture is driven by the minimization of the total mechanical energy of the system, defined as the sum of elastic and surface energies:

$$E(\boldsymbol{u},\Gamma) = \int_{\Omega\setminus\Gamma} w(\boldsymbol{\epsilon}(\boldsymbol{u}),\Gamma)\, dV + g_c \int_{\Gamma} dS \tag{6}$$

where Γ is the set of cracks contained in Ω, $w(\boldsymbol{\epsilon}) = \frac{1}{2}\boldsymbol{\epsilon} : \mathbb{C} : \boldsymbol{\epsilon}$ is the elastic energy, and g_c is the fracture toughness of the supposedly isotropic material. In order to avoid numerical difficulties associated to real cracks as material discontinuities, the approach put forward by **Bourdin, 2008** and developed by **Miehe et al., 2010**, is followed. In this approach, cracks are represented by a continuous "phase field", damage-like internal variable, and material discontinuities are replaced by strong gradients of the phase field. In this respect, it is a non-local (i.e. gradient based) damage model involving a characteristic length, seen as a material constant. Then, Eqn. (6) is replaced by:

$$E(\boldsymbol{u},\phi) = \int_{\Omega} g(\phi) w(\boldsymbol{u})\, dV + g_c \int_{\Omega} \left(\frac{\phi^2}{2\ell} + \frac{\ell}{2} \left| \nabla \phi \right|^2 \right) dV \tag{7}$$

where $g(\phi)$ is an elastic softening function. In this expression, the surface integral appearing in Eqn. (6) has been replaced by a volume integral incorporating the gradient of the phase field ϕ. Taking the variational derivative of (7) with respect to the displacement $\boldsymbol{u}$ yields simply the equilibrium equation, whereas taking its variational derivative with respect to the phase field ϕ gives:

$$\begin{aligned} \frac{g_c}{2\ell}\phi - \frac{\ell}{2}\mathrm{div}(\mathrm{g}_c\, \nabla\phi) &= -\mathrm{g}'(\phi) w(\boldsymbol{\epsilon}(\boldsymbol{u})) \quad \text{on } \Omega \\ \nabla\phi.\boldsymbol{n} &= 0 \quad \text{on } \partial\Omega \end{aligned} \tag{8}$$

The left member of Eqn. $(8)_1$ is a diffusion term, thus allowing to smear the cracks, whereas the right member can be interpreted as a driving force for the (smeared) cracking process. Notice that at this stage, if unloading occurs, w decreases, and so does ϕ, meaning crack regression (or healing). To avoid this unphysical situation, **Miehe et al., 2010** modify Eqn. $(8)_1$ as follows:

$$\frac{g_c}{2\ell}\phi - \frac{\ell}{2}\mathrm{div}(\mathrm{g}_c\,\nabla\phi) = -\mathrm{g}'(\phi)\mathcal{H}(\boldsymbol{\epsilon}(\boldsymbol{u})) \tag{9}$$

where $\mathcal{H}(\boldsymbol{\epsilon}(t)) = \max_{0\le s\le t} w(\boldsymbol{\epsilon}(s))$, thereby forbidding the driving force to decrease.

A second modification is necessary to handle a series of effects, referred to as “unilateral effects”, namely (i) that cracking is not possible under compressional loads, (ii) that open cracks may close back but crack lips cannot interpenetrate, and (iii) that crack closure is accompanied by a recovery of normal stress transmission and thus of local elastic properties, at least partly. Following **Miehe et al., 2010**:

$$w(\boldsymbol{\epsilon}) = g(\phi)w^+(\boldsymbol{\epsilon}) + w^-(\boldsymbol{\epsilon}) \tag{10}$$

and:

$$w^\pm(\boldsymbol{\epsilon}) = \frac{\lambda}{2}\left\langle \mathrm{tr}\boldsymbol{\epsilon}\right\rangle_\pm^2 + \mu\mathrm{tr}(\boldsymbol{\epsilon}_\pm^2) \tag{11}$$

where $\boldsymbol{\epsilon}^+$ (respectively $\boldsymbol{\epsilon}^-$) is the positive (resp. negative) part of the strain tensor, and $\left\langle x\right\rangle_\pm = \frac{1}{2}\ x \pm \left|x\right|$.

The stress tensor is modified accordingly to:

$$\boldsymbol{\sigma} = g(\phi)\left[\lambda\left\langle \mathrm{tr}\boldsymbol{\epsilon}\right\rangle_+ + 2\mu\boldsymbol{\epsilon}_+\right] + \left[\lambda\left\langle \mathrm{tr}\boldsymbol{\epsilon}\right\rangle_- + 2\mu\boldsymbol{\epsilon}_-\right] \tag{12}$$

and the phase field equation (9) becomes:

$$\frac{g_c}{2\ell}\phi - \frac{\ell}{2}\mathrm{div}(\mathrm{g}_c\,\nabla\phi) = -\mathrm{g}'(\phi)\mathcal{H}^+(\boldsymbol{\epsilon}(\boldsymbol{u})) \tag{13}$$

where $\mathcal{H}^+(\boldsymbol{\epsilon}(t)) = \max_{0\le s\le t} w^+(\boldsymbol{\epsilon}(s))$.

In order to handle the strong anisotropy of the TATB crystal, Eqn. (13) can be modified as follows (see, in particular, **Clayton and Knapp, 2015**):

$$\frac{g_c}{2\ell}\phi - \frac{\ell}{2}g_c\mathrm{div}(\boldsymbol{\omega}.\nabla\phi) = -\mathrm{g}'(\phi)\mathcal{H}(\boldsymbol{\epsilon}^+(\boldsymbol{u})) \tag{14}$$

where $\boldsymbol{\omega}$ is a second order symmetric tensor accounting for the dependence of the surface energy to the crystallographic orientation. This tensor can be identified on the molecular dynamics simulation results of **Bidault and Pineau, 2018**. The unilateral effect in the anisotropic case must also be accounted for, following for example **Nguyen et al., 2017**).

6.2. FFT integration algorithm

Summarizing, the model consists of a set of two partial differential equations, namely the equilibrium equation and Eqn. (14). They are solved with the following staggered algorithm. For a given loading step, equilibrium is first solved at fixed phase field, by using the classical "direct scheme" fixed point algorithm proposed by **Moulinec and Suquet, 1994**. Eqn. (12) is then solved at fixed strain by using the following finite difference approximation:

$$\mathrm{div}(\boldsymbol{\omega}.\nabla\phi) \approx \frac{1}{h^2}\sum_{\alpha}\omega_{\alpha}\Big[\phi(\boldsymbol{x}+h\boldsymbol{e}_{\alpha})+\phi(\boldsymbol{x}-h\boldsymbol{e}_{\alpha})-2\phi(\boldsymbol{x})\Big] \tag{16}$$

where h is the voxel size, and the ω_{α} are the principal values of the tensor $\boldsymbol{\omega}$. The softening function is chosen as $g(\phi)=(1-\phi)^2$, such that the approximation of Eqn. (14) is linear with respect to ϕ, allowing the conjugate gradient method to be used.

The choice of a staggered algorithm oblige to use small loading steps, especially when phase field increments are large, which is the case during crack propagation. Besides, especially when ϕ is close to 1, the elastic tensor $(1-\phi)^2\mathbb{C}$ almost vanishes, and it is often useful to transform Eqn. (10) into:

$$w(\boldsymbol{\epsilon}) = \Big[g(\phi)+k\Big]w(\boldsymbol{\epsilon}^{+})+w(\boldsymbol{\epsilon}^{-}) \tag{17}$$

with $k \ll 1$, in order to regularize the problem and accelerate convergence.

6.3. Validation

At the present time, only 2D computations have been performed. A simulation is first done to compare the results of the above-described FFT algorithm with the finite element one of **Miehe et al., 2010**, in the isotropic case, and using the same material constants (Lamé constants $\lambda = 121.5\ \mathrm{GPa}$ and $\mu = 80.77\ \mathrm{GPa}$, and fracture toughness $g_c = 2.7\ \mathrm{J.m^{-2}}$). The unit cell is a homogeneous isotropic notched 140×140 pixels square domain (see Fig. 7a), loaded in mode I (tension), with a 10^{-6} axial strain loading step. Finally, an array of 2 void pixels is added on the lateral boundary of the domain to enforce uniaxial stress loading. Recall that periodic boundary conditions imply the unit cell to be periodically replicated along both directions.

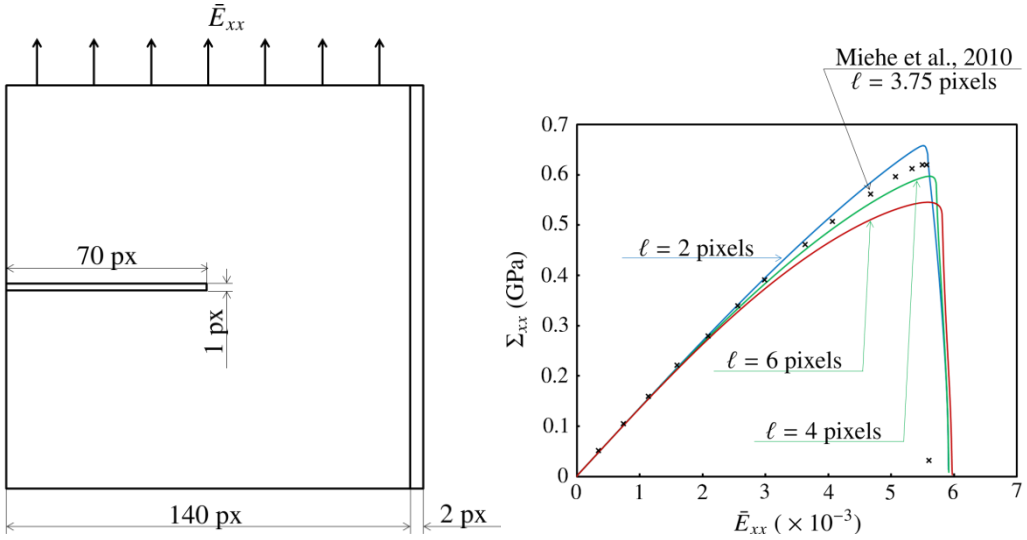

Fig. 7: Notched homogeneous isotropic domain loaded in mode I.

a (left): geometrical configuration – **b** (right): FFT simulation results for various values of ℓ, and comparison with the finite element results of **Miehe et al., 2010** (crosses, same material parameters, $\ell = 3.75\ \mathrm{pixels}$).

Fig. 7b shows the results parameterized par the characteristic length ℓ, expressed in pixels. The main point is that the characteristic length has a noticeable influence on the peak stress. This is mainly due to the fact that the model has no threshold: the phase field ϕ grows from the beginning of loading. As noticed by several authors, ℓ must therefore be seen as a full material parameter, not only a regularizing one.

The same configuration is used to validate the account of the unilateral effect (Fig. 8). With the same parameters, the notched domain is first loaded in tension (blue curve in Fig. 8). As soon as the crack begins to propagate, the domain is unloaded, then loaded in compression (red curve in Fig. 8). Upon unloading, a softened linear response is observed, whereas elastic stiffness recovery is clearly displayed upon reverse (compressional) loading: the slope of the initial part of loading and of reverse loading are the same (dashed black line in Fig. 8).

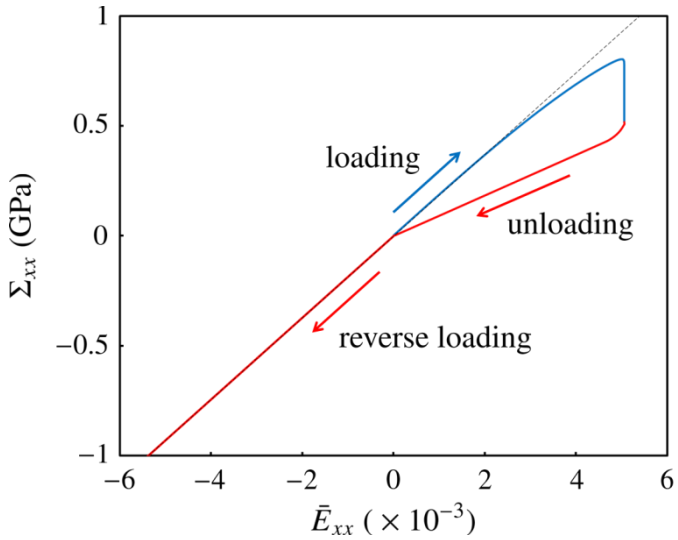

Fig. 8: Loading, unloading and reverse loading exhibiting elastic recovery induced by the unilateral effect.

6.4. Preliminary polycrystal simulations

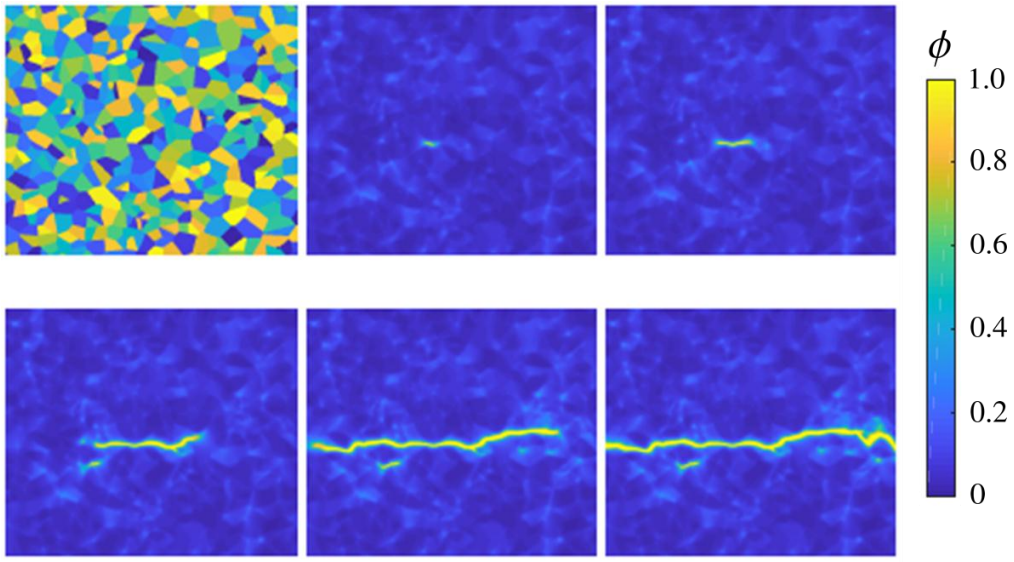

Fig. 9: Tensile loading of a polycrystal, showing multiple crack nucleation and propagation to fracture.

A first 2D (plane strain) simulation consists in mode I uniaxial stress tensile loading in the vertical direction of a large Voronoi polycrystal with anisotropic elasticity, Eqn. (4), and isotropic phase field law, Eqn (9), with no unilateral effect. The evolution of the phase field is illustrated in Fig. 9. It shows that a first crack nucleates, then propagates, and keeps propagating while secondary cracks nucleate, but do not propagate. The final

crack is horizontal, i.e. normal to the loading direction, in the average, and exhibits a relatively strong roughness.

A second exploratory simulation consists in submitting a small Voronoi polycrystal (200 grains) to a purely thermal loading, namely cooling from ambient temperature to -200°C, with anisotropic thermoelasticity, Eqn. (4), anisotropic phase field law, Eqn. (14), including the unilateral effect, (**Nguyen et al., 2017**), but with isotropic fracture toughness. For this exploratory simulation, a relatively high resolution is chosen (500x500 pixels), and all the components of the macroscopic stress tensor are prescribed to zero. It should be kept in mind that the results are not directly comparable to a thermal expansion experiment, for the simulations are plane strain two-dimensional ones. The phase field at three temperatures is displayed in Fig. 10, showing the applicability of the model to pure thermal loading.

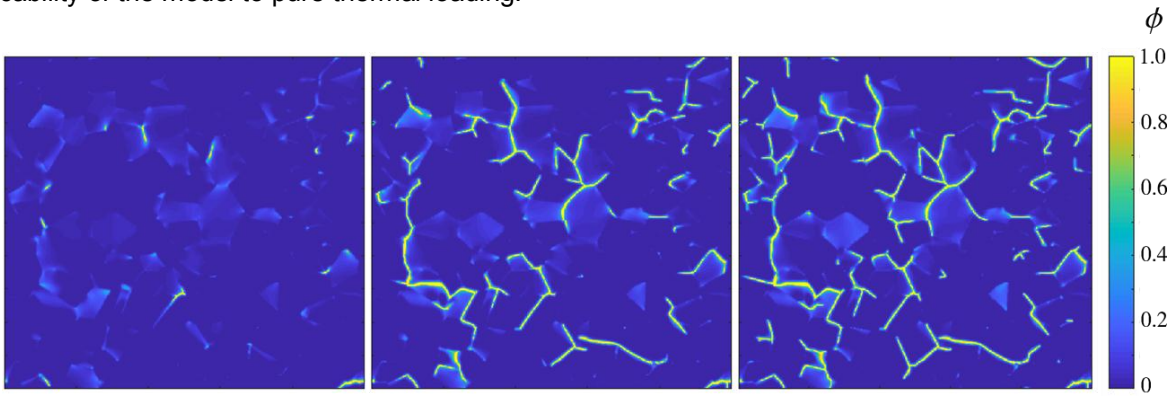

Fig. 10: Exploratory simulation for thermal loading (cooling) of a 100 grains Voronoi polycrystal for $\Delta T = -160$ (left), -240 (middle), and $-320°C$ (right, fictitious temperatures).

Fig. 11 displays the macroscopic thermal strain along an arbitrary axis, versus temperature difference, resulting from this simulation. Although the comparison can only be qualitative, this plot shows clearly a nonlinear response below a temperature threshold, and the reduced slope of the re-heating phase, in a way very similar to what is observed experimentally (Fig. 2b).

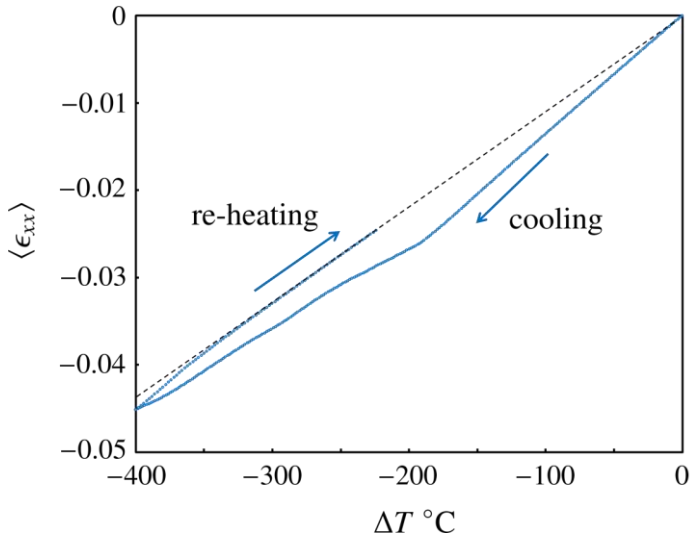

Fig. 11: Macroscopic thermal strain vs. temperature difference, showing the non-linearity threshold and the reduction of the thermal expansion coefficient (dashed black line) during heating.

7. Mean-field approach: self-consistent method

7.1. Brief description of the method

Besides the full-field approach outlined above, some mean-field work has also been performed, due to its relative simplicity and numerical efficiency. Briefly, the method is based on the celebrated result of **Eshelby, 1957**. Consider an infinite homogeneous elastic matrix containing an ellipsoidal elastic inclusion, and apply a

remote macroscopic stress $\boldsymbol{\Sigma}$. Then, the stress $\boldsymbol{\sigma}^i$ and strain $\boldsymbol{\epsilon}^i$ fields in the inclusion are homogeneous, and:

$$\boldsymbol{\epsilon}^i - \boldsymbol{E} = -\mathbb{S}^* : \boldsymbol{\sigma}^i - \boldsymbol{\Sigma} \tag{18}$$

where $\boldsymbol{E}$ is the macroscopic strain tensor, and $\mathbb{S}^*$ is an "interaction" tensor depending only on the form of the inclusion and the properties of the matrix.

Consider now a heterogeneous multiphase (polycrystalline) infinite elastic domain loaded remotely by the same macroscopic stress $\boldsymbol{\Sigma}$. Assume that each α-th phase can be seen as a homogeneous ellipsoidal elastic inclusion of volume fraction c_α and elastic properties $\mathbb{C}^\alpha$. Then, one can superimpose a single Eshelby problem for each phase by considering the matrix to have the effective properties of the multiphase domain: this is the self-consistent approximation (**Hill, 1965**). Then, if all the inclusions have the same interaction tensor (same form and same matrix properties), the effective elastic properties are given by:

$$\tilde{\mathbb{S}} = \left\langle (\mathbb{S} + \mathbb{S}^*)^{-1} \right\rangle^{-1} - \mathbb{S}^* \tag{19}$$

where $\tilde{\mathbb{S}}$ is the effective elastic compliance (the inverse of the effective elastic tensor), and $\langle x \rangle = \int_\Omega x \, dV = \sum_\alpha c_\alpha x^\alpha$ is the volume average of the quantity x, supposed uniform per phase, and $\mathbb{S}$ is the elastic compliance of each phase. In the case of a polycrystal, a "phase" is defined as the domain over which the crystallographie orientation, and thus the elastic tensor, is uniform. Eqn. (19) is implicit, since $\mathbb{S}^*$ depends on the effective properties, and must be solved iteratively. Likewise, the effective thermal expansion tensor is given by:

$$\tilde{\boldsymbol{\alpha}} = \left\langle (\mathbb{S} + \mathbb{S}^*)^{-1} : (\mathbb{S} + \mathbb{S}^*) : \boldsymbol{\alpha} \right\rangle \tag{20}$$

When applied to the above-mentioned perfect polycrystal, the self-consistent method provides the same results as the full-field approach, within 1% for the effective bulk modulus, 2% for the shear modulus, and 3% for the volumetric thermal expansion coefficient, which is quite satisfactory for quasi-instantaneous predictions.

7.2. Statistical description of local fields

As can be seen from Eqn. (16), the only microstructural data entering the method is the phase volume fractions and their crystallographic orientations. This is a rather crude description of a microstructure, and means that local interactions are not described accurately, but only in an average sense. As shown by Eqn. (16), the local fields are given as phase averages. However, a refinement of the self-consistent method, proposed by **Bobeth and Diener, 1987**, allows the calculation of the cross second moments of the fields in each phase. When comparing the phase averages and cross second moments of the fields predicted by the self-consistent and by the full-field FFT methods, the match is once again excellent, within the same accuracy as above.

This suggests a method for predicting field statistical histograms from the self-consistent method (**Willot et al., 2019**). The simplest way of building a probability distribution function knowing its average and cross second moments is to assume a Gaussian form. This is postulated here in the form of a vector-valued normal distribution in each phase as follows:

$$\mathcal{P}_{\boldsymbol{\epsilon}}^\alpha(\boldsymbol{t}) = \frac{1}{\sqrt{\left|\boldsymbol{A}_{\boldsymbol{\epsilon}}^\alpha\right|(2\pi)^6}} \exp\left(-\frac{1}{2} (\boldsymbol{t} - \boldsymbol{M}_{\boldsymbol{\epsilon}}^\alpha)^t . (\boldsymbol{A}_{\boldsymbol{\epsilon}}^\alpha)^{-1} . (\boldsymbol{t} - \boldsymbol{M}_{\boldsymbol{\epsilon}}^\alpha) \right) \tag{21}$$

where $\mathcal{P}_{\boldsymbol{\epsilon}}^{\alpha}(\boldsymbol{t})$ is the probability that the field $\boldsymbol{\epsilon}$ takes the value $\boldsymbol{t}$ in the α-th phase, $\boldsymbol{M}_{\boldsymbol{\epsilon}}^{\alpha} = \left\langle \boldsymbol{\epsilon} \right\rangle_{\alpha}$ is the 6-valued vector of the phase-averages of strains in the α-th phase, and $\boldsymbol{A}_{\boldsymbol{\epsilon}}^{\alpha}$ is the 6x6 covariance matrix, defined as:

$$\boldsymbol{A}_{\boldsymbol{\epsilon}}^{\alpha} = \left\langle (\boldsymbol{\epsilon} - \boldsymbol{M}_{\boldsymbol{\epsilon}}^{\alpha}) \otimes (\boldsymbol{\epsilon} - \boldsymbol{M}_{\boldsymbol{\epsilon}}^{\alpha}) \right\rangle_{\alpha} = \boldsymbol{\Pi}_{\boldsymbol{\epsilon}}^{\alpha} - \boldsymbol{M}_{\boldsymbol{\epsilon}}^{\alpha} \otimes \boldsymbol{M}_{\boldsymbol{\epsilon}}^{\alpha} \tag{22}$$

where $\boldsymbol{\Pi}_{\boldsymbol{\epsilon}}^{\alpha} = \left\langle \boldsymbol{\epsilon} \otimes \boldsymbol{\epsilon} \right\rangle_{\alpha}$ is the 6x6 matrix of crossed second moments of strains in the α-th phase. From the postulated phase distribution functions, the distribution function for the entire polycrystal can be reconstructed as follows:

$$\mathcal{P}_{\boldsymbol{\epsilon}}(\boldsymbol{t}) = \sum_{\alpha} c_{\alpha} \mathcal{P}_{\boldsymbol{\epsilon}}^{\alpha}(\boldsymbol{t}) \tag{23}$$

where c_{α} is the volume fraction of the α-th phase. The results are compared to the distributions obtained with full-field simulations for hydrostatic loading ($\bar{E}_{xx} = \bar{E}_{yy} = \bar{E}_{zz} = 1$, other components equal to zero) in Fig. 11a, and for shear loading ($\bar{E}_{xy} = 0.5$,other components equal to zero) in Fig. 11b.

The agreement is quite satisfactory, which shows that, despite the crudeness of the microstructure description used for the mean-field approximation, accurate effective properties statistical distributions of local fields are obtained. Therefore, its extension towards cracked polycrystalline microstructures (**Willot et al., 2019**) is being sought presently, but is beyond the scope of the present paper.

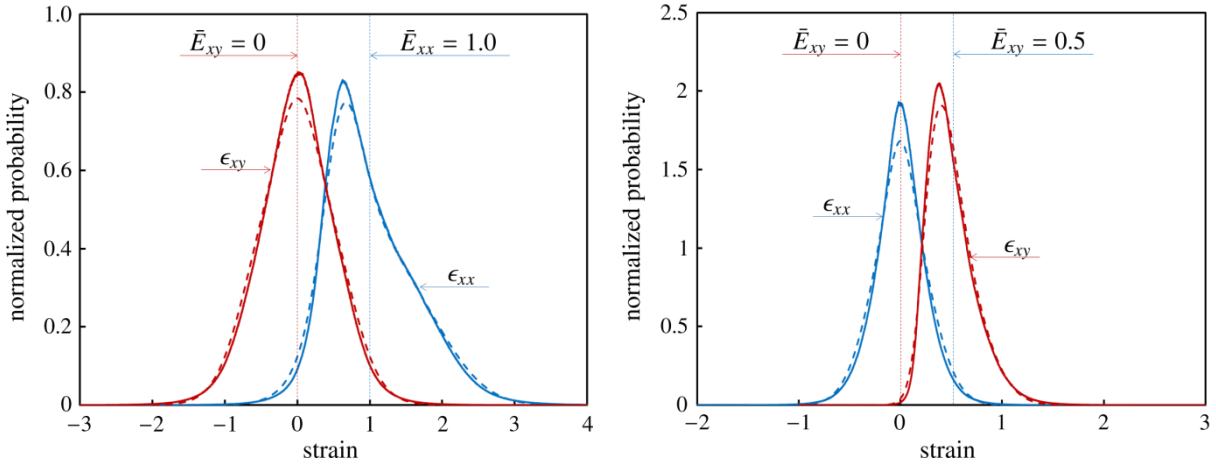

Fig. 11: Distribution functions of some strain fields in the polycrystal
continuous: from FFT full-field computations - dashed: reconstructed from self-consistent calculations
a (left): hydrostatic loading – **b** (right): shear loading.

7.3. Extension to binder (linear) viscoelasticity

The account of the effect of the binder viscoelasticity has been undertaken via the mean-field approach as follows. Assuming that linear (non-ageing) viscoelasticity, the binder stress-strain relationship reads:

$$\sigma_{ij}(t) = \int_0^t \mathbb{L}_{ijkl}(t-s)\dot{\epsilon}(s)ds = \frac{d}{dt}\ \mathbb{L}_{ijkl} * \epsilon_{kl} \tag{24}$$

where $\mathbb{L}$ is the relaxation function, and $*$ stands for the convolution product. Using the Laplace-Carson transformation, Eqn. (24) transforms into:

$$\sigma^*_{ij}(p) = L^*_{ijkl}(p)\epsilon^*_{kl}(p) \tag{25}$$

Therefore, any viscoelastic problem may be reformulated as an elastic symbolic one (**Hashin, 1965**). Hence, any elastic homogenization theory may be extended to account for linearly viscoelastic constituents. In the case of forced harmonic steady-state loading such as that applied experimentally in Dynamic Mechanical Analysis (DMA), a harmonic overall strain $\overline{\boldsymbol{\epsilon}}(t) = \boldsymbol{E}^* e^{i\omega t}$ is applied, and $p = i\omega$, where ω is the angular frequency. Then, the homogenization problem may be stated as follows:

$$\begin{cases} \sigma^*_{ij}(\boldsymbol{x}, \mathrm{i}\,\omega) = \mathrm{L}^*_{ijkl}(\boldsymbol{x}, \mathrm{i}\,\omega)\epsilon^*_{kl}(\boldsymbol{x}, \mathrm{i}\,\omega) \\ \sigma^*_{ij,j} = 0 \\ \left\langle \epsilon^*_{ij} \right\rangle = \bar{E}^*_{ij} \end{cases} \tag{26}$$

with periodic boundary conditions. Eqn. (26) shows that in this case, an elastic homogenization must be performed for each angular frequency (**Hashin, 1970**).

It will first be assumed that the binder follows a Zener (or “standard viscoelastic solid”) model:

$$\boldsymbol{\sigma}(t) + \tau\dot{\boldsymbol{\sigma}}(t) = \mathbb{L}^0 : \boldsymbol{\epsilon}(t) + \tau\mathbb{L}^0 : \dot{\boldsymbol{\epsilon}}(t) \tag{27}$$

where $\mathbb{L}^0$ and $\mathbb{L}^\infty$ are the elastic glassy (instantaneous) and relaxed (rubbery) tensors, and τ is a characteristic relaxation time. The corresponding complex relaxation function $\mathbb{L}^*$ of the Zener binder is:

$$\mathbb{L}^*(i\omega) = \mathbb{L}^\infty + (\mathbb{L}^0 - \mathbb{L}^\infty)\frac{i\omega\tau}{1 + i\omega\tau} \tag{28}$$

The first step consists in finding the best possible mean-field theory to account for the topology of the binder, i.e. thin layers around TATB grains. The above-described standard self-consistent, the Mori-Tanaka (**Mori and Tanaka, 1973**), and the generalized self-consistent (**Herve and Zaoui, 1990**) models have been considered, and their results compared to those obtained by FFT simulations. For the latter, the microstructure was a composite of poly-disperse isotropic elastic spheres embedded in an isotropic viscoelastic Zener continuous matrix with a volume fraction of inclusions of 50% (see Fig. 12a). The bulk relaxation of the matrix is moreover supposed negligible, such that shear viscoelasticity only is considered, The results are shown in Fig. 12b. The self-consistent model provides a strong overestimation of FFT results, and underestimates the drop of the storage modulus (i.e. the real part of the relaxation function) at low frequencies. The inverse trend is observed for Mori-Tanaka, while the predictions of the generalized self-consistent model are quite correct. It should be noticed, however, that (i) the quality of the approximation gets poorer as the volume fraction of filler increases, and (ii) that this model is unable to deal with anisotropic filler.

Space-time interactions between constituents induce a so-called “long memory effect” (see e.g. **Suquet, 1987**), such that the effective relaxation function $\tilde{\mathbb{L}}^*$ involves in general a continuum of effective relaxation times:

$$\tilde{\mathbb{L}}^*(i\omega) = \tilde{\mathbb{L}}^\infty + \int_0^\infty \mathcal{G}(\tau)\frac{i\omega\tau}{1 + i\omega\tau}\,d\tau \tag{29}$$

and does not obey a Zener constitutive law. The second step of the approach is then to determine how Eqn. (29) can be best approximated. This is usually done by using a so-called Prony series, in the form:

$$\tilde{\mathbb{L}}^*(i\omega) = \tilde{\mathbb{L}}^\infty + \sum_{k=1}^{n} \mathcal{G}(\tau_k)\frac{i\omega\tau_k}{1 + i\omega\tau_k}\,d\tau \tag{30}$$

and the question is how to identify the discrete characteristic times and moduli. For this purpose, the use of exact relationships will be sought, instead of using the usual empirical collocation method (see e.g. **Schapery, 1961**). In the case of composites of Maxwell constituents, **Suquet, 2012** showed the existence of four theoretical exact relationships, thus reducing the number of material constants to identify. **Gallican et al., 2018** extended the validity of these relationships to any Zener viscoelastic constituents. Therefore, the minimum value for n is 2, which only leaves one free material constant. For example, one of the characteristic times can be set to that of the Zener binder.

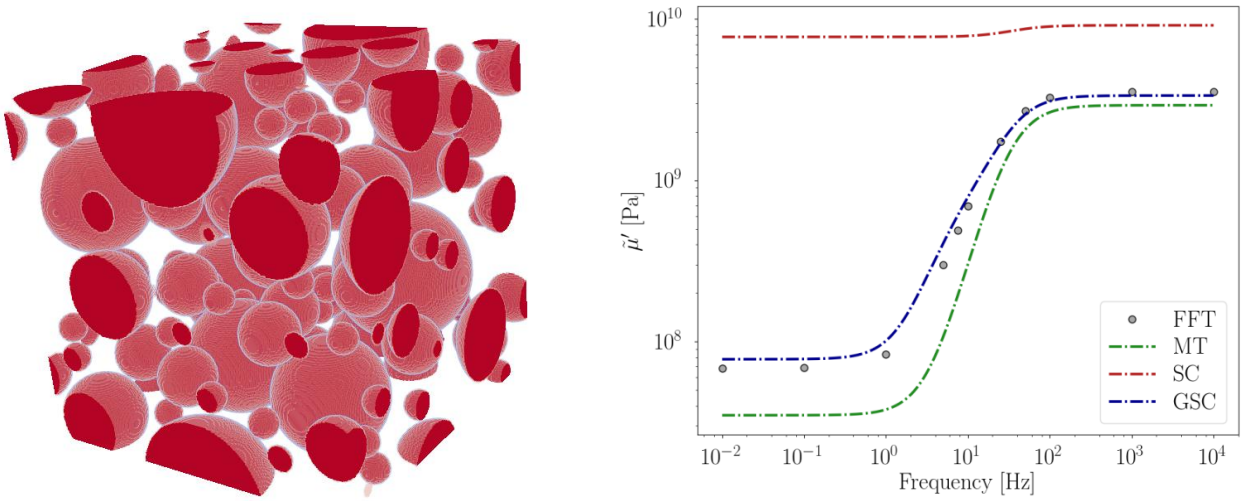

Fig. 12: **a** (left): the 50% vol. fraction composite of elastic spheres embedded in a Zener matrix used for FFT computations – **b** (right): comparison between the homogenized shear storage modulus (real part of the complex relaxation function) predicted by the Mori-Tanaka (MT), self-consistent (SC) and generalized self-consistent (GSC) mean-field theories and full-field FFT computations (**Gallican et al., 2018**).

The present approach suffers a major drawback: the Zener model, involving a single relaxation time, provides a poor representation of the viscoelastic relaxation of real polymers. For this reason, the approach outlined above is being extended by proposing a fractional derivative Zener description (**Bagley and Torvik, 1983**) of the viscoelastic binder, in the following form:

$$\boldsymbol{\sigma}(t) + \tau^{\alpha} \frac{d^{\alpha}\boldsymbol{\sigma}}{dt^{\alpha}}(t) = \mathbb{L}^{0} : \boldsymbol{\epsilon}(t) + \tau^{\alpha}\mathbb{L}^{0} : \frac{d^{\alpha}\boldsymbol{\epsilon}}{dt^{\alpha}}(t) \tag{31}$$

with $0 \leq \alpha \leq 1$. The corresponding complex relaxation modulus is given by:

$$\mathbb{L}^{*}(i\omega) = \mathbb{L}^{\infty} + (\mathbb{L}^{0} - \mathbb{L}^{\infty}) \frac{(i\omega\tau)^{\alpha}}{1 + (i\omega\tau)^{\alpha}} \tag{32}$$

Recently, **Gallican and Brenner, 2019** extended the validity of the four exact relationships to fractional Zener constituents, and showed that the effective relaxation function is given by:

$$\tilde{\mathbb{L}}^{*}(i\omega) = \tilde{\mathbb{L}}^{\infty} + \int_{0}^{\infty} \mathcal{G}(\tau) \frac{(i\omega\tau)^{\alpha}}{1 + (i\omega\tau)^{\alpha}} d\tau \tag{33}$$

Therefore, the entire approach can be extended to fractional linear viscoelasticity. The next steps will be, in a near future, to identify a fractional Zener viscoelastic law for the real binder of the explosive at stake, to compare the predictions of the generalized self-consistent model to the actual experimental relaxation function of the explosive, and finally to provide an accurate approximation for the latter.

8. Conclusion and ongoing work

The approach followed here is ambitious. The first results obtained in the purely linear thermoelastic context have already provided some new knowledge about a TATB-based pressed explosive composition. Within this limited context, it appears clearly that the TATB crystal anisotropy is the first crucial element on the way to a better understanding of the thermomechanical behavior of this material. Going further, however, needs that irreversible and nonlinear mechanisms be accounted for. Among those, namely micro-cracking, binder viscoelasticity and crystal plasticity, the accent has been put here on the first one, by developing a phase field description of the fracture process. The developments are under way, and the first results are promising, although only the transgranular cracking process has been accounted for up to now. The intergranular one will be introduced, and results should be available soon.

Treating the question of the binder viscoelasticity via full-field simulations is a difficult task, due to the fact that the binder topology is that of locally very thin layers, thus needing very high spatial resolution for full-field simulations. This is the reason why it is being studied using the mean-field approach.

The study of the effects of TATB crystal non-elastic deformation is also a difficult task because, to our knowledge, no data are available at present. The understanding of such mechanisms has therefore been undertaken, in view of developing an adequate model to be incorporated in the above-described full-field FFT numerical tool. This work is described in the companion paper.

It has been shown that, although the exact fields are not predicted by the mean-field method, their histograms can be reproduced accurately. This is an interesting finding, in particular towards the prediction of extreme values (i.e. maxima and minima) of stress fields, that are important physical quantities that trigger nonlinear threshold phenomena such as cracking and plasticity. The method has so far been applied to the perfect polycrystal only, and is presently being extended to microcracking.

Up to now, full-field and mean-field predictions have only been compared to macroscopic experimental data. It is highly desirable to acquire microstructure-scale data as well. Dedicated experiments are being designed for this purpose. In the foreseeable future, they will be limited to optical and SEM observations during uniaxial compression experiments, and should provide 2D strain field data via microstructure-scale digital image correlation. Since computational fields are only available on virtual microstructures, the comparison with experimental fields can only be performed on a statistical basis. Besides, the question of crystal orientations within the explosive composition must also be raised. Up to now, those orientations have been assumed to be random, but experimental data are highly desirable, and some dedicated work should be undertaken soon.

9. References

A. Ambos, F. Willot, D. Jeulin, H. Trumel (2015), *Numerical modeling of the thermal expansion of an energetic material*, Int. J. Solids Struct., **60-61**, 125-139.

B. S. Anglin, R. A. Lebensohn, A. D. Rollett, (2014), *Validation of a numerical method based on Fast Fourier transforms for heterogeneous thermoelastic materials by comparison with analytical solutions*, Comput. Mat. Sci., **87**, 209-217.

R. L. Bagley, P. J. Torvik (1983), *A theoretical basis for the application of fractional calculus to viscoelasticity*, J. Rheol., **27**, 201-210.

D. Bedrov, O. Borodin, G. D. Smith, T. D. Sewell, D. M. Dattelbaum, L. L. Stevens (2009), *A molecular dynamics simulation study of crystalline 1,3,5-triamino-2,4,6-trinitrobenzene as a function of pressure and temperature,* J. Chem. Phys., **131**, 224703.

X. Bidault, N. Pineau (2018), *Impact of surface energy on the shock properties of granular explosives*, J. Chem. Phys., **148**, 034704.

M. Bobeth and G. Diener (1987), *Static and thermoelastic field fluctuations in multiphase composites*, J. Mech. Phys. Solids, **35**, 137-149.

B. Bourdin, G. A. Francfort, J.-J. Marigo, J.-J. (2008), *The variational approach to fracture*, J. Elasticity, **91**, 5-148.

B. Budiansky, R. J. O'Connell, R. J. (1976), *Elastic moduli of a cracked solid*, Int. J. Solids Struct., **12**, 81-97.

J. D. Clayton, J. Knap (2015), *Phase field modeling of directional fracture in anisotropic polycrystals*, Comput. Mat. Sci., **98**, 158-169.

J. D. Eshelby, (1957), *The determination of the elastic field of an ellipsoidal inclusion, and related problems*, Proc. R. Soc. Lond., **241**, 376-396.

G. A. Francfort, J.-J. Marigo (1998), *Revisiting brittle fracture as an energy minimization problem*, J. Mech. Phys. Solids, **46**, 1319-1342.
V. Gallican, R. Brenner, P. Suquet (2017), *Exact asymptotic relations for the effective response of linear viscoelastic heterogeneous media*, C. R. Mecanique, **345**, 742-751.

V. Gallican., R. Brenner, H. Trumel (2018), *Homogenization estimates for the time harmonic response of particulate viscoelastic composites*, 16th European Mechanics of Materials Conference, 26-28/03/2018, Nantes, France.

J.-B. Gasnier, F. Willot, H. Trumel, B. Figliuzzi, D. Jeulin, M. Biessy (2015), *A Fourier-based numerical homogenization tool for an explosive material*, Mat. & Tech., **103**, 308.

J.-B. Gasnier, F. Willot, H. Trumel, D. Jeulin, J. Besson (2018a), *Thermoelastic properties of microcracked polycrystals. Part I: Adequacy of Fourier-based methods for cracked elastic bodies*, Int. J. Solids Struct., **155**, 248-256.

J.-B. Gasnier, F. Willot, H. Trumel, D. Jeulin, M. Biessy (2018b)), *Thermoelastic properties of microcracked polycrystals. Part II: The case of jointed polycrystalline TATB*, Int. J. Solids Struct., **155**, 257-274.

R. H. Gee, A. Maiti, L. E. Fried (2007), *Mesoscale modeling of irreversible volume growth in powders of anisotropic crystals*, Appl. Phys. Lett., **90**, 254105.

Z. Hashin (1965), *Viscoelastic behavior of heterogeneous media*, J. Appl. Mech.*,* **32**, 630-636.

Z. Hashin (1970), *Complex moduli of viscoelastic composites-I. General theory and application to particulate composites*, Int. J. Solids Structures, **6**, 539-552.

E. Herve, A. Zaoui (1990), *Modelling the effective behavior of non-linear matrix-inclusion composites*, Eur. J. Mech./A. Solids, **9**, 505-515.

R. Hill (1965), *A self-consistent mechanics of composite materials*, J. Mech. Phys. Solids, **13**, 213-222.

J. R. Kolb, H. F. Rizzo (1979), *Growth of 1,3,5-triamino-2,4,6-trinitrobenzene. I. Anisotropic thermal expansion*, Prop. Expl. Pyrotech., **4**, 10-16.

V. D. Le, M. Gratton, M. Caliez, A. Frachon, D. Picart (2010), *Experimental mechanical characterization of plastic-bonded explosives*, J. Mat. Sci., **45**, 5802-5813.

C. Miehe, M. Hofacker, F. Welschinger (2010), *A phase field model for rate-independent crack propagation: Robust algorithmic implementation based on operator splits*, Comput. Methods Appl. Mech. Engrg., **199**, 2765-2778.

T. Mori, K. Tanaka (1973), *Average stress in matrix and average elastic energy of materials with misfitting inclusions*, Acta Metall., **21**, 571-574.

H. Moulinec, P. Suquet (1994), *A fast numerical method for computing the linear and nonlinear properties of composites*, C.R. Acad. Sci. Paris II, **318**, 1417-1423.

T.-T. Nguyen, J. Réthoré, J. Yvonnet, M.-C. Baietto (2017), *Multi-phase-field modeling of anisotropic crack propagation for polycrystalline materials*, Comput. Mech., **60**, 289-314.

P. Palmas, T. Botzanowski, M. Guerain, A. Forzy, E. Bruneton, G. Delrio (2016), *Size determination of porosity inclusions in an organic solid material by 1H NMR diffusion and SEM-FIB experiments: the TATB case*, J. Phys. Chem., **B120**, 4152-4259.

D. Picart, J.-L. Brigolle, J.-L. (2010), *Characterization of the viscoelastic behaviour of a plastic-bonded explosive*, Mat. Sci. Engng. A, **527**, 7826-7831.

B. W. Rosen, Z. Hashin, Z (1970), *Effective thermal expansion coefficients and specific heats of composite materials*, Int. J. Engrg. Sci., **8**, 157-173.

R. A. Schapery (1961), *A simple collocation method for fitting viscoelastic models to experimental data*, California Institute of Technology report nr. SM-61-23A, Pasadena, USA.

J. Sun, B. Kang, C. Xue, Y. Liu, Y. Xia, X. Liu, W. Zhang (2010), *Crystal state of 1,3,5-triamino-2,4,6-trinitrobenzene (TATB) undergoing thermal cycling process*, J. Energetic Mat., **28**, 189-201.

P. Suquet (1987), *Elements of homogenization for inelastic solid mechanics*, In: Sanchez-Palencia, E., Zaoui, A. (eds.), Homogenization techniques for composite media, Lecture Notes in Physics, **272**, Springer Verlag, New York, 193–278.

P. Suquet (2012), *Four exact relations for the effective relaxation function of linear viscoelastic composites*, C. R. Mecanique, 340, 387-399.

D. G. Thompson, C. Woznick, R. DeLuca (2018), *The volumetric coefficient of thermal expansion of PBX 9502*, Report nr. LA-UR-18-22138, Los Alamos National Laboratory, USA.

F. Willot, H. Trumel, D. Jeulin (2018), *The thermoelastic response of cracked polycrystals with hexagonal symmetry*, Phil. Mag., DOI: 10.1080/14786435.2018.1547432.

F. Willot, R. Brenner, H. Trumel (2019), *Elastostatic field distributions in polycrystals and cracked media*, submitted to Proc. R. Soc. Lond.